Gain-of-Function Variant p.Pro2555Arg of von Willebrand Factor Increases Aggregate Size through Altering Stem Dynamics

Volker Huck[1,2,*]   Po-Chia Chen[3,*]   Emma-Ruoqi Xu[4,*]   Alexander Tischer[5]   Ulrike Klemm[6]
Camilo Aponte-Santamaría[7,8]   Christian Mess[1]   Tobias Obser[1]   Fabian Kutzki[9,10]   Gesa König[6]
Cécile V. Denis[11]   Frauke Gräter[8,9]   Matthias Wilmanns[4,12]   Matthew Auton[5]   Stefan W. Schneider[1]
Reinhard Schneppenheim[6]   Janosch Hennig[3,**]   Maria A. Brehm[1,**]

[1] Department of Dermatology and Venereology, Center for Internal Medicine, University Medical Center Hamburg-Eppendorf, Hamburg, Germany
[2] Experimental Dermatology, Medical Faculty Mannheim, Heidelberg University, Mannheim, Germany
[3] Structural and Computational Biology Unit, European Molecular Biology Laboratory, Heidelberg, Germany
[4] European Molecular Biology Laboratory, Hamburg Unit, Hamburg, Germany
[5] Division of Hematology, Mayo Clinic, Rochester, Minnesota, United States
[6] Department of Pediatric Hematology and Oncology, University Medical Center Hamburg-Eppendorf, Hamburg, Germany
[7] Max Planck Tandem Group in Computational Biophysics, University of los Andes, Bogotá, Colombia
[8] Interdisciplinary Center for Scientific Computing, Heidelberg University, Heidelberg, Germany

Address for correspondence Maria A. Brehm, Department of Dermatology and Venereology, University Medical Center Hamburg-Eppendorf, Martinistrasse 52, 20246 Hamburg, Germany (e-mail: m.brehm@uke.de).

Janosch Hennig, Structural and Computational Biology Unit, EMBL Heidelberg, Meyerhofstrasse 1, 69117 Heidelberg, Germany (e-mail: janosch.hennig@embl.de).

[9] Molecular Biomechanics Group, Heidelberg Institute for Theoretical Studies, Heidelberg, Germany
[10] Institute of Physical Chemistry, Karlsruhe Institute of Technology, Karlsruhe, Germany
[11] Laboratory of Hemostasis, Inflammation and Thrombosis, Institut National de la Santé et de la Recherche Médicale UMR_1176, Université Paris-Saclay, Le Kremlin-Bicêtre, France
[12] University Medical Center Hamburg-Eppendorf, Hamburg, Germany

Abstract

Keywords
► von Willebrand factor
► hypercoagulability
► GPIIb/IIIa

The multimeric plasma glycoprotein (GP) von Willebrand factor (VWF) is best known for recruiting platelets to sites of injury during primary hemostasis. Generally, mutations in the *VWF* gene lead to loss of hemostatic activity and thus the bleeding disorder von Willebrand disease. By employing cone and platelet aggregometry and microfluidic assays, we uncovered a platelet GPIIb/IIIa-dependent prothrombotic gain of function (GOF) for variant p.Pro2555Arg, located in the C4 domain, leading to an increase in platelet aggregate size. We performed complementary biophysical and structural investigations using circular dichroism spectra, small-angle X-ray scattering, nuclear magnetic resonance spectroscopy, molecular dynamics simulations on the single C4 domain, and dimeric wild-type and p.Pro2555Arg constructs. C4-p.Pro2555Arg retained the overall structural conformation with minor populations of alternative

---

* *These authors contributed equally to this study.*
** *Co-senior authors.*

conformations exhibiting increased hinge flexibility and slow conformational exchange. The dimeric protein becomes disordered and more flexible. Our data suggest that the GOF does not affect the binding affinity of the C4 domain for GPIIb/IIIa. Instead, the increased VWF dimer flexibility enhances temporal accessibility of platelet-binding sites. Using an interdisciplinary approach, we revealed that p.Pro2555Arg is the first VWF variant, which increases platelet aggregate size and shows a shear-dependent function of the VWF stem region, which can become hyperactive through mutations. Prothrombotic GOF variants of VWF are a novel concept of a VWF-associated pathomechanism of thromboembolic events, which is of general interest to vascular health but not yet considered in diagnostics. Thus, awareness should be raised for the risk they pose. Furthermore, our data implicate the C4 domain as a novel antithrombotic drug target.

Introduction

Von Willebrand factor (VWF) plays a key role in hemostasis by mediating platelet adhesion to the site of vascular injury and by protecting factor VIII from rapid clearance in the circulation.[1,2] It is well accepted that mutations generally lead to various VWF dysfunctions that result in the most common bleeding disorder, von Willebrand disease (VWD). Severity is variable, depending on the many particular molecular defects of this multidomain (►**Fig. 1A**) and multifunctional protein.[3–5]

However, in recent years increasing evidence has been gathered that VWF can also be regarded as a prothrombotic factor. Stroke[6] and thrombotic complications in sepsis,[7] inflammation and infections, such as COVID-19,[8] are associated with high plasma levels of VWF.

We have recently described the first gain-of-function (GOF) variant of VWF which exhibits shear-dependent prothrombotic characteristics. This common VWF variant, p.Phe2561Tyr (rs35335161), plays a significant role in premature and repeated events of myocardial infarction (MI) in younger women as shown in a cohort of the Ludwigshafen Risk and Cardiovascular Health Study.[9,10] p.Phe2561Tyr is located in the VWF C4 domain (►**Fig. 1B**), harboring the RGD-binding sequence for platelet receptor glycoprotein (GP) IIb/IIIa.[11] Our functional and structural studies have indicated that the Tyr2561 allele shifts the onset of aggregation to lower shear rates compared to Phe2561-VWF.[10,12] The GPIIb/IIIa-binding RGD motif is situated at the tip of a flexible and extended loop region within a β-hairpin, which is one of the two layers of β-sheets in the first subdomain (SD1) of C4. p.Phe2561Tyr is located in the second subdomain (SD2) instead, close to the C-terminus of the domain, remote from the RGD motif (►**Fig. 1B**) and does not affect direct binding to GPIIb/IIIa under static conditions. Instead, the Tyr2561 allele causes a minor population with a different SD1/SD2 hinge conformation, and alters the tertiary structure of dimers which could support dimer stem opening at lower shear rates.[12] Previously, shear-dependent functions were shown for the VWF A1 and A2 domains. Our data now indicate that the C-domain-encompassing stem region of VWF also functions in response to shear force (►**Fig. 1C**). However, deeper insight into the biophysical properties of this part of the VWF

protein as well as the mechanisms by which it influences platelet binding is lacking. We thus strived to better elucidate the functional properties of the VWF stem region and performed a database search for further SNPs in the C4 domain, and chose to investigate the rather rare missense variant p. Pro2555Arg (rs915754316; minor allele frequency 0.00007; https://www.ncbi.nlm.nih.gov/projects/SNP/snp_ref.cgi? rs=915754316) due to its proximity to Phe2561 in the VWF C4 domain structure (►**Fig. 1B**). Since VWF sequencing is generally only performed in patients with bleeding symptoms to date, no clinical phenotype has been reported for this variant yet.

To explore possible functional consequences of p. Pro2555Arg, we performed extensive functional, structural, and biophysical studies and show that this variant possesses prothrombotic properties different from p.Phe2561Tyr. p. Pro2555Arg is the first VWF variant which increases platelet aggregate size (AS). The underlying mechanism is shear-dependent and independent of fibrinogen (fb).

These data show that mutations in the VWF stem region can enhance VWF's prothrombotic properties and suggest that more such variants exist representing a novel risk factor for thromboembolic disease.

Methods

Protein Expression, Purification, and Quantification

HEK293 cell lines, stably expressing either full-length wild-type VWF (wtVWF), p.Pro2555Arg, both variants after co-transfection, or control variant p.Asp2509Glu with an inactivated RGD sequence, were derived from transiently transfected HEK293 cell clones as described.[10,13]

Wt and p.Pro2555Arg D4N-CK (residues 1873–2813, UniProt P04275) were recombinantly expressed in HEK293T cells using the pXLG vector, which contains an N-terminal secretory signal peptide PSG1 (pregnancy-specific β1-glycoprotein 1) and a C-terminal His$_6$-tag. The cells were transfected transiently using polyethylenimine, and the D4N-CK protein was secreted into the medium. Ni-Sepharose Excel beads (GE Healthcare) were mixed with the harvested medium and the protein was eluted with 300 mM imidazole. The eluted protein was dialyzed
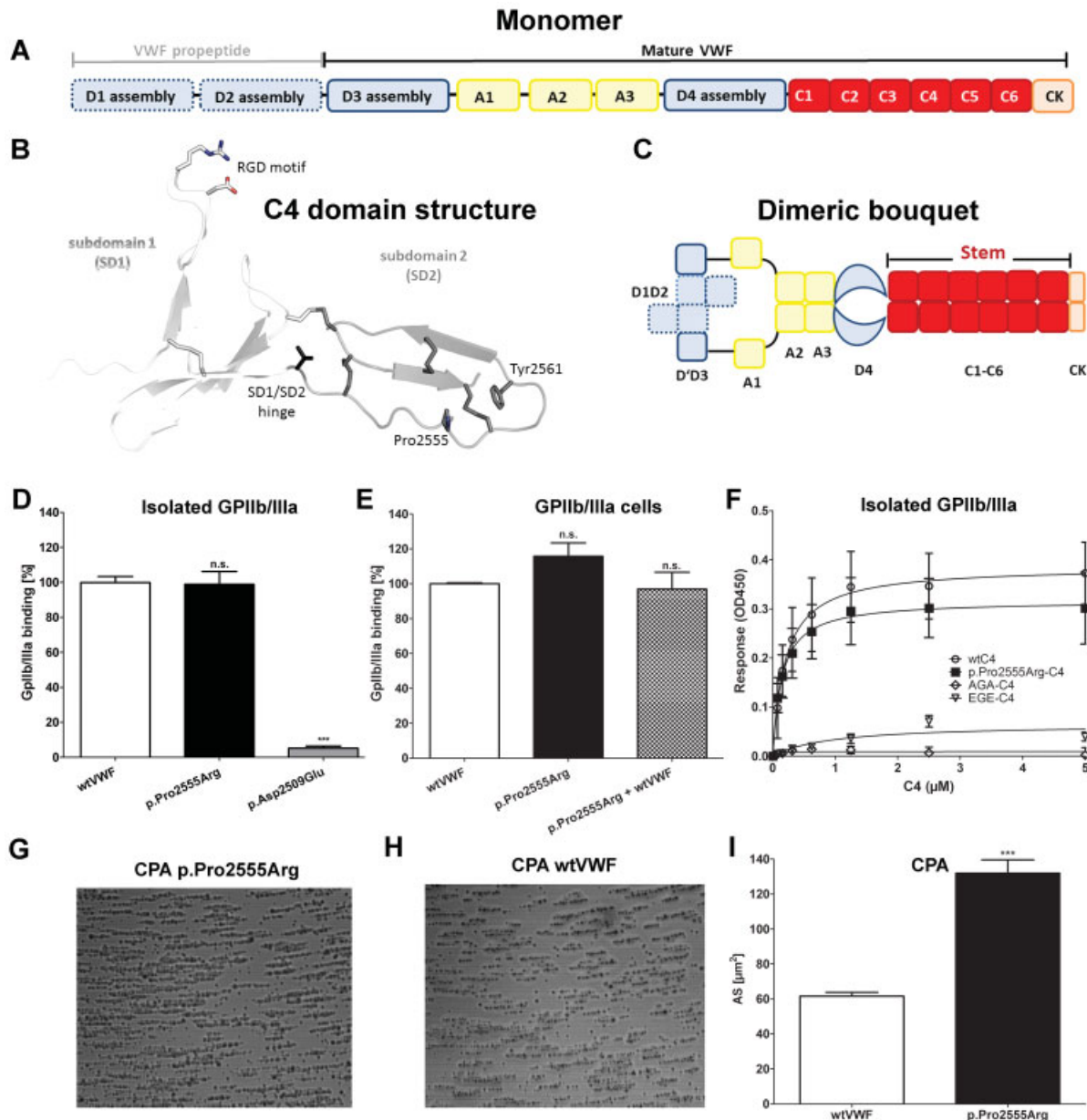
Fig. 1 VWF and C4 domain structure and VWF-variant:platelet integrin binding under static and flow conditions. (**A**) Schematic representation of the domain structure of a VWF monomer. (**B**) Structure of the C4 domain showing the two subdomains SD1 (*light gray*) and SD2 (*darker gray*), with the GPIIb/IIIa binding RGD motif, SD1/SD2 hinge residue, Pro2555, Tyr2561, and disulfides shown as sticks. (**C**) Schematic representation of a VWF dimer in the bouquet conformation with a closed C-domain stem region. (**D**) Recombinant wtVWF (*white*), p.Pro2555Arg (*black*), and negative control p.Asp2509Glu (*gray*), in which the C4 RGD sequence is inactivated, were incubated in microtiter wells with immunoadsorbed GPIIb/IIIa purified from platelets. Bound VWF was detected using an HRP-conjugated anti-VWF antibody. Presented is % binding relative to wtVWF set to 100%. (**E**) Immunoadsorbed recombinant wtVWF (*white*), p.Pro2555Arg (*black*), and both variants co-expressed (*checkered*) were incubated with HEK293 cells stably expressing a constitutively active mutant of GPIIb/IIIa. Bound cells were detected using mouse anti-GPIIb/IIIa and a polyclonal HRP-coupled goat anti-mouse secondary antibody. The data represent the mean values ± SEM of three independent measurements. Unpaired t-test: ***$p < 0.001$. (**F**) Recombinant single wtC4 domain (*circles*), p.Pro2555Arg (*squares*), negative controls AGA-C4 (p.Arg2507Ala_Asp2509Ala, *diamonds*), and EGE-C4 (p.Arg2507Glu_Asp2509Glu, *triangles*) in increasing concentrations were incubated with immobilized GPIIb/IIIa. Mean values ± SEM of three to four independent experiments are shown. (**G–I**) To investigate platelet aggregation under shear flow conditions, whole blood was washed, and plasma was replaced with VWF-deficient VWD type 3 plasma. After addition of 25 µm/mL of either wtVWF (*white*) or p.Pro2555Arg (*black*) (I), cone and plate(let) aggregometry (CPA) was performed at 1,800 s^{-1} for 2 minutes. Aggregates were stained using May-Grünwald solution. Seven pictures per test were recorded employing a build-in microscope and camera and analyzed using the IMPACT-R image analyzer software. One representative image for p.Pro2555Arg and wtVWF are shown in (G) and (H), respectively. Each test was performed in duplicates. Mean values ± SEM of three independent experiments are shown. Unpaired t-test: ***$p < 0.001$). n.s.: not significant; SEM, standard error of the mean; VWD, von Willebrand disease; VWF, von Willebrand factor; wtVWF, wild-type von Willebrand factor.

against phosphate buffer, before being concentrated and purified using Superdex 200 Increase 10/300 GL (GE Healthcare) in 20 mM HEPES pH 7.5, 150 mM NaCl, 1 mM CaCl$_2$, 1 mM MgCl$_2$.

Wt and p.Pro2555Arg C1-CTCK (residues 2256–2813) domain constructs were expressed as fusion proteins containing a His-tag as previously described.[10] Secreted proteins were loaded onto a XK26 column packed with Nickel-NTA resin (GE Healthcare, Marlborough, Massachusetts, United States) using a BioCAD Sprint HPLC system (PerSeptive BioSystems, Framingham, Massachusetts, United States). Column-bound proteins were washed with 250 mL of 25 mM imidazole and eluted with 1 M imidazole (both solutions: 1M NaCl and 100 mM Tris/HCl, pH 7.4), followed by dialysis for 40 hours into 2×4 L of 150 mM NaCl, 10 mM sodium phosphate, pH 7.4.

Wt and p.Pro2555Arg single C4 domains (residues 2497–2577) were generated using similar methods as previously described.[12] Samples for nuclear magnetic resonance (NMR) were prepared in 20 mM sodium phosphate pH 6.5, for circular dichroism (CD) in 10 mM sodium phosphate pH 7.4, for small-angle X-ray scattering (SAXS) in 20 mM Tris-HCl pH 7.5, 150 mM NaCl. Sample conditions fulfilling method-dependent requirements necessitated the use of different buffer components and pH values.

Static GPIb and GPIIb/IIIa Binding Assays

Comparative binding of recombinant full-length wtVWF, p. Pro2555Arg, and negative control variant p.Asp2509Glu to isolated GPIIb/IIIa was assessed by an enzyme-linked-immunosorbent assay (ELISA) using GPIIb/IIIa isolated from platelets[14] and by a cell-based assay, employing HEK293 cells expressing constitutively active platelet GPIIb/IIIa at their surface. Development and validation of the latter assay were previously described.[15] Binding of the single C4 domain to GPIIb/IIIa was investigated as previously described.[12] VWF: GPIbα binding measurements were performed as previously described.[16] All binding assays were performed under non-saturating conditions with equal concentrations of wtVWF and the respective variants, allowing the detection of eventual increased binding of GOF mutants.

Cone and Plate(let) Aggregometry

Cone and plate(let) aggregometry (CPA) was performed employing the IMPACT-R device (Matis Medical Inc., Beersel, Belgium) with cones and polystyrene wells as provided in the Impact-R Test kit, according to the manufacturer's instructions. Whole blood was washed as previously described[17] to remove the donor's plasma VWF, which was replaced by plasma from an adult patient with VWD type 3, who has a nondetectable VWF antigen (VWF:Ag) but normal fb levels (determined by radial immunodiffusion). The same batch of plasma was used for all CPA experiments; therefore, the fb concentration was always 3.94 g/L. Then either wtVWF or p. Pro2555Arg was added and CPA was performed at 1,800 s^{-1} for 2 minutes. In previous studies we determined the optimal concentration for sufficient aggregate formation of wtVWF in CPA experiments, when using recombinant protein in washed blood, to be 25 µg/mL. To receive comparable data, we always used this same concentration for wt and mutant VWF. Aggregates were stained using May-Grünwald solution. Seven pictures/test were recorded employing a build-in microscope and camera and analyzed using the IMPACT-R image analyzer software. Each sample was measured in duplicates in three independent experiments.

Microfluidic Assays

Functional characterization of VWF-induced collective network formation[18] under high-shear conditions was performed in air-pressure-driven microfluidic channels (Bioflux, San Francisco, California, United States; width: 350 µm, height: 70 µm) coated with 50 µg/mL of either recombinant wtVWF, p.Pro2555Arg, or p.Asp2509Glu as previously described.[19] Citrated whole blood was washed and platelets fluorescently stained as published.[19] Absence of fb after following the washing protocol was confirmed by radial immunodiffusion. The concentration was below the detection limit of 0.5 g/L. Washed blood, including 200,000 platelets per µL, 45% washed hematocrit, and 10 µg/mL of either wtVWF, p.Pro2555Arg (with or without addition of 1.3 µL/mL abciximab [ReoPro, stock concentration: 2 mg/mL; Centocor, now Janssen Biotech Inc., Horsham, Pennsylvania, United States)], or p.Asp2509Glu, was subjected to shear rates in the range of 500–4,000 s^{-1} (with a nominal shear rate precision of 36 s^{-1}), which were increased in stages of 500 s^{-1} every minute during experiments. For the experiments in the presence of fb, washed hematocrit and platelets were brought to the original volume with the same VWD type 3 plasma also used for the CPA experiments and 10 µg/mL of the respective VWF variants was added. Live cell fluorescence movies were taken with eight frames/s. At least four independent experiments were performed for each group. For image analysis and rolling AS quantification, we used the ZEN software (Zeiss AG, Jena, Germany) and the open-source software ImageJ (V. 1.46r, National Institute of Health, Bethesda, Maryland, United States).[20] The study was conducted in conformity with the Declaration of Helsinki and to the International Conference on Harmonization of Technical Requirements for Registration of Pharmaceuticals for Human Use Guidelines (www.ich.org), accessed in August 2018. Blood donation of volunteers was approved by the Ethics Committee of the Medical Faculty Mannheim, Heidelberg University (Mannheim, Germany). Appropriate informed consent was obtained from all subjects.

Circular Dichroism Spectra

All protein concentrations were determined on a UV2101PC spectrophotometer (Shimadzu, Kyoto, Japan) after centrifugation of the solutions at $60,000 \times g$ at 4°C for 10 or 20 minutes to remove potential protein aggregates. The extinction coefficients used for C4 and C1-CTCK were 11,260 and 41,515 L mol^{-1} cm^{-1} and were calculated from the number of tryptophan and tyrosine residues.

CD spectra were recorded at 25°C on an Aviv Biomedical Model 420SF CD spectrophotometer. Spectra in the far-ultraviolet (far-UV) range (200–260 nm) were recorded using a 1 mm quartz cell with an integration time of 60 seconds and band- and step-widths of 1 nm. Near-UV CD spectra were recorded using either a 10 cm cylindrical quartz cell (for both C1CTCK proteins) or a 0.2 or 1 cm quartz cell (both for wtVWF

and p.Pro2555Arg C4, respectively). The integration time was 60 or 120 seconds and band- and step-widths were 1 nm. All spectra were corrected for the signal of the corresponding buffer and converted to mean ellipticity per amino acid residue.

Small-Angle X-Ray Scattering

SAXS data were collected at EMBL beamline P12 at the PETRA III storage ring (DESY, Hamburg, Germany) using a 2M Pilatus pixel detector (DECTRIS) with a distance of 3.1 m. D4N-CK constructs were measured at 0.6 to 1.2 mg/mL, in 20 mM HEPES pH 7.5, 150 mM NaCl, 1 mM CaCl$_2$, 1 mM MgCl$_2$. Single C4 constructs were measured at 3.6 to 4.6 mg/mL in 20 mM Tris-HCl pH 7.5, 150 mM NaCl. Data collection was performed with standard batch-mode setup at 20°C with a total exposure time of 1.5 seconds (recorded as 30×50 ms frames) and subtracted by matching buffer scattering. Analysis of the scattering data was performed using programs from the ATSAS 2.8.4 package.[21] The forward scattering $I(s)$ is plotted against s, where $s = 4\pi\sin\theta/\lambda$, with 2θ being the scattering angle and λ the X-ray wavelength (1.24 nm; 10 keV). The radii of gyration (R_g) were calculated from the Guinier approximation using PRIMUS.[22] GNOM[23] was used to obtain the pairwise distribution function $p(r)$, and to calculate the maximum particle dimension (D_{max}).

NMR Spectroscopy

Resonance assignment of backbone amide proton/nitrogen resonances of p.Pro2555Arg-C4 was achieved by transferring wtVWF-C4 assignments[12] and tracing peak shifts with regard to peak positions in wtVWF-C4. The introduced arginine in p. Pro2555Arg-C4 and surrounding residues exhibited large chemical shift perturbations compared to wtVWF-C4, thus causing ambiguities in peak tracing. These ambiguities were resolved using sequential H_N-$H_{\alpha-1}$ nuclear Overhauser effects (NOEs) derived from a ^{15}N-NOESY-HSQC experiment.

The NMR relaxation experiments on wtVWF-C4 from Xu et al (2019)[12] were repeated for p.Pro2555Arg, and a summary is presented here. All experiments were carried out at 298 K on Bruker Avance III NMR spectrometers (600, 700, and 800 MHz) and a Bruker DRX NMR spectrometer (500 MHz); 600 and 800 MHz spectrometers are equipped with cryogenic triple resonance gradient probe heads. The buffer composition was the same as for wt (20 mM sodium phosphate, pH 6.5) and a protein concentration of 250 µM was used. Measurements of R_1, R_2, and ^{1}H-^{15}N heteronuclear NOE experiments for the VWF-C4 p.Pro2555Arg variant were acquired using standard pulse sequences and relaxation delays specified in ►Table 1. To assess the micromillisecond dynamics for certain residues, Carr–Purcell–Meiboom–Gill (CPMG)[24,25] relaxation dispersion experiments were conducted using a previously published pulse sequence.[26] Effective fields of $v_{CPMG} = 1/(4\tau_{CP})$ were used, where $2\tau_{CP}$ is the interval between refocusing pulses with frequencies shown in ►Table 1. All spectra were processed with NMRPipe[27] and analyzed using Sparky[28] and PINT.[29,30]

ROTDIF[31] was employed to determine the diffusion tensor from R_2/R_1 ratios and used to compute the rotational correlation time τ_c. After excluding residues with hetNOE values <0.65, the axially symmetric diffusion model exhibited the minimal best fit.

Molecular Dynamics Simulations

Atomistic and explicit-solvent molecular dynamics (MD) simulations were conducted using GROMACS software,[32] version 5.1.x or 2016.2. The simulation methodology used here is based on Xu et al.[12] Note that the published NMR ensemble (6FWN.pdb) corresponds to the NMR-detectable extended conformation. To improve sampling efficiency, the wtVWF-C4 trajectory data produced by Xu et al[12] was used instead to include both extended and bent conformations as sampling templates.

Two independent MD protocols were performed in this study. In one protocol, 20 snapshots were drawn and manually mutated to form p.Pro2555Arg using Visual Molecular Dynamics software.[33] This formed the starting ensemble for CHARMM22* simulations. In the other protocol, 14 snapshots were drawn and manually mutated using Pymol,[34] forming the starting ensemble for Amber99sb-ildn* simulations. Relevant simulation parameters are summarized in ►Supplementary Table S1 (available in the online version).

Results

p.Pro2555Arg Exhibits GOF Characteristics Only under Shear Flow Conditions

Functional characterization of recombinant full-length wtVWF and p.Pro2555Arg multimers was carried out by

Table 1 A summary of parameters used to conduct p.Pro2555Arg NMR experiments

	Spectrometer frequency (MHz)	Relaxation delays (ms)
R_1	500, 600, 700, and 800	20, 20, 50, 100, 150, 250, 400, 500, 650, 800, 1,000, 1,300, and 1,600 ($N = 13$)
R_2	500, 600, 700, and 800	16, 16, 32, 48, 64, 80, 96, 112, 128, 160, 192, 224, and 256 ($N = 13$)
^{1}H–^{15}N hetNOE	500, 600, 700, and 800	n.a. ($N = 2$)
		Refocusing pulse frequency (Hz)
CPMG	600 and 800	33, 66, 100, 133, 200, 266, 333, 400, 466, 533, 600, 666, 800, and 933 ($N = 14$)

Abbreviations: CPMG, Carr–Purcell–Meiboom–Gill; NMR, nuclear magnetic resonance.

measuring binding to isolated platelet GPIIb/IIIa in an ELISA format and, additionally, by a cell-based assay using HEK293 cells, expressing the constitutively active GPIIb/IIIa variant p.Thr588Asn.[33] In both static assays, p.Pro2555Arg did not show a significant difference in GPIIb/IIIa binding compared to wtVWF (►**Fig. 1D, E**). Also, for the single C4-domain construct, used for structural investigation, normal GPIIb/IIIa binding was observed (►**Fig. 1F**). As expected, control variants with mutations in the RGD sequence were unable to bind GPIIb/IIIa (►**Fig. 1D, F**) and VWF:GPIbα binding was unaltered by p.Pro2555Arg (►**Supplementary Fig. S1A**, available in the online version).

To determine if p.Pro2555Arg exhibits shear-dependent alterations, we performed CPA. Washed blood was supplemented with VWD type 3 plasma, which has no detectable VWF:Ag but a normal fb concentration (3.94 g/L). Then either recombinant wtVWF or p.Pro2555Arg was added and CPA was performed. As shown in ►**Fig. 1(G–I)**, the platelet AS was increased by about 100% in the presence of p.Pro2555Arg (►**Fig. 1G, I**) compared to wtVWF at the same concentration (►**Fig. 1H–I**). Such a prothrombotic GOF characteristic was previously only observed for VWF variant p.Phe2561Tyr.[10] In the CPA setup, the presence of the control mutant p.

Asp2509Glu, in which the GPIIb/IIIa-binding RGD sequence is inactivated, also exhibited a somewhat increased platelet AS compared to the presence of wtVWF (►**Supplementary Fig. S1B**, available in the online version).

Our findings are in accordance with a previous study by Wu et al,[34] showing that fb can compensate for VWF in platelet crosslinking, when the VWF-RGD sequence is disturbed.

Since presence of fb is required for platelet aggregate adhesion in CPA assays, we next performed a microfluidic assay which does not require fb, to gain more insights into the mechanism by which p.Pro2555Arg increases the size of platelet aggregates (►**Fig. 2**). At lower shear rates of 500 and 2,000 s^{-1}, both variants behaved similarly, showing only single platelets rolling along the VWF-biofunctionalized surface. The first platelet-decorated VWF fibers emerged at the channel surface at 2,000 s^{-1} (►**Fig. 2A**, colored spots in left panels). Above a critical shear rate of 4,000 s^{-1}, fiber-like structures partially detached and induced the origin of large reversible VWF–platelet collective network aggregates rolling along the surface,[35,36] which were significantly increased in size when p.Pro2555Arg was present in the reconstituted blood (►**Fig. 2A**, top) at the same physiological concentration
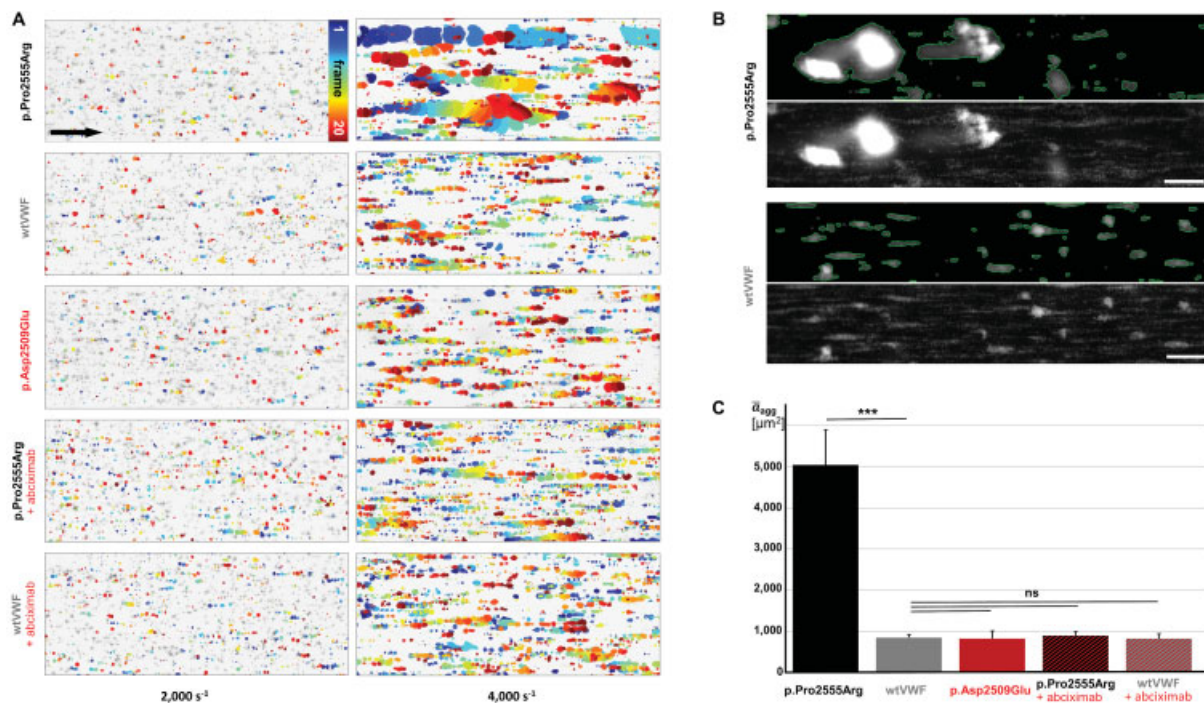
Fig. 2 Characteristics of VWF-induced collective network formation of wtVWF and p.Pro2555Arg at indicated shear rates. (**A**) Each image represents a composition of 20 sequential frames of a live-cell fluorescence movie taken at a frequency of eight frames per second. By subtracting identical pixels among frames, a color-coded addition of these differential images from frame 0 (*blue*) to frame 20 (*red*) along the color scale, combined with the inverted gray-scaled background image of the start frame, allows precise detection and motion tracking of VWF-induced collective networks. Therefore, only moving networks are displayed in color enabling an exact determination of the critical shear rate. While the critical shear rate for rolling aggregate formation is the same as for p.Pro2555Arg (*upper row*) and wtVWF (*second row*), p.Pro2555Arg shows significantly increased aggregate sizes. The mutant p.Asp2509Glu does neither affect the critical shear rate, nor the aggregate size compared to wtVWF (*third row*). Nevertheless, by inhibition of GPIIb/IIIa via abciximab, the GOF effect by p.Pro2555Arg is completely abolished (*fourth row*), while addition of abciximab to wtVWF does not change its aggregate formation behavior (*bottom row*). The *black arrow* indicates the flow direction and corresponds to 100 µm. One example out of at least four independent experiments is shown. (**B** and **C**) Computer-assisted quantification of the collective network size at the critical shear rate demonstrates an about sixfold increase in size of the detected rolling aggregates for p.Pro2555Arg in comparison to wtVWF. Panel (B) shows one exemplary image used for the quantification. The *white scale bars* correspond to 100 µm. (C) Mean values ± SEM of at least four independent experiments are shown. Unpaired t-test: ***$p < 0.001$. GOF, gain of function; SEM, standard error of the mean; VWF, von Willebrand factor; wtVWF, wild-type von Willebrand factor.

of 10 µg/mL as wtVWF. Computer-assisted quantification of collective network size at a shear rate of 4,000 s^{-1}, the critical shear rate for rolling aggregate formation as shown in ►Fig. 2A, demonstrates an increase of the mean area of detected rolling aggregates from 853 µm^2 for wtVWF to 5,041 µm^2 in the presence of p.Pro2555Arg (►Fig. 2B, C). These data confirm a shear-dependent GOF effect by p.Pro2555Arg (see also ►Video 1) different from p.Phe2561-Tyr, which showed aggregates of the same size as wtVWF but already at 2,000 s^{-1}.[10] In the absence of the plasmatic VWF fraction, neither platelet-binding fibers nor collective networks are formed.[10] Interestingly, in our microfluidic setting mimicking the early phase of rolling aggregate formation, mutant p.Asp2509Glu did not exhibit any significant difference, neither in the critical shear rate nor in the size of aggregates, compared to wtVWF. This finding indicates that the initial occurrence of aggregate formation does not necessarily require VWF–GPIIb/IIIa interactions. To test the hypothesis that p.Pro2555Arg nevertheless mediates the increase in AS via a GPIIb/IIIa-associated mechanism, we next added the GPIIb/IIIa-blocking antibody abciximab to the microfluidic experiments and found that, upon inhibition of GPIIb/IIIa, the GOF effect by p.Pro2555Arg was completely abolished (►Fig. 2A, compare first and fourth rows).

Video 1

Characteristics of VWF-induced collective network formation of p.Pro2555Arg. Excerpts of a representative live cell fluorescence movie (bottom) with the corresponding computer assisted analysis of the collective network size (top) for p.Pro2555Arg. The movie was taken at a frequency of eight frames per second. During the experiment, the shear rate was increased in stages of 500 s-1 up to 4,000 s-1. For better illustration, excerpts at shear rates of 1,000, 2,000, 3,000 and 4,000 s-1 are depicted separated by fading out. At the critical shear rate of 4,000 s-1 huge collective networks of p.Pro2555Arg and platelets are formed rolling along the surface of the channel. The current shear rate in s-1 is stated in the upper left ('rate:'), the current time frame as indicated ('f:'). Note that the exemplary image shown in ►Fig. 2B was taken at frame 1,140.
Online content including video sequences viewable at: https://www.thieme-connect.com/products/ejournals/html/10.1055/a-1344-4405.

To test whether fb plays a role in this GOF effect of p.Pro2555Arg, we further repeated the microfluidic experiment in the presence of fb by employing the VWD type 3 plasma used for the CPA experiments. We found a significant increase in size of reversibly formed VWF–platelet collective network aggregates in both the absence and the presence of physiological fb concentration above the same critical shear rate of 4,000 s^{-1} (from 1,143 µm^2 for wtVWF to 4,610 µm^2 in the presence of p.Pro2555Arg, see ►Supplementary Fig. S2,

available in the online version). These data indicate that the GOF effect of p.Pro2555Arg is not promoted by fb and further suggest that p.Pro2555Arg does not lead to enhanced aggregation and platelet activation with subsequent fb release. This observation is in line with previous findings by Constantinescu-Bercu et al,[37] who showed that VWF binding to platelet GPIbα via the VWF-A1 domain leads to platelet "priming," which is characterized by GPIIb/IIIa activation without full platelet activation.[37–39] In conclusion, p.Pro2555Arg seems to mediate increased agglutination during this priming phase of platelet activation in a fb-independent manner. Furthermore, the GOF effect of p.Pro2555Arg is also present at normal plasma fb antigen and could therefore be physiologically relevant in a carrier of the p.Pro2555Arg mutation.

Circular Dichroism Spectra Reveal That p.Pro2555Arg Affects the Dimeric Structure of the C-Terminal Stem Region

To assess the impact of p.Pro2555Arg on the secondary and tertiary structures of the monomeric single C4 domain and the dimeric domain construct C1-CTCK, far- and near-UV CD spectra were recorded for wt and p.Pro2555Arg C4 and C1-CTCK (►Fig. 3). Within the single C4 domain, p.Pro2555Arg has no detectable effect on secondary and tertiary structures as the far- and near-UV CD spectra are identical to those of the wt protein (►Fig. 3, top panels). The far-UV CD spectrum of C4 shows a maximum at 230 nm and a minimum at 206 nm for both wtVWF and p.Pro2555Arg. The overall shape of the spectrum is typical for a protein that is dominated by β-strand and random coil structural elements.
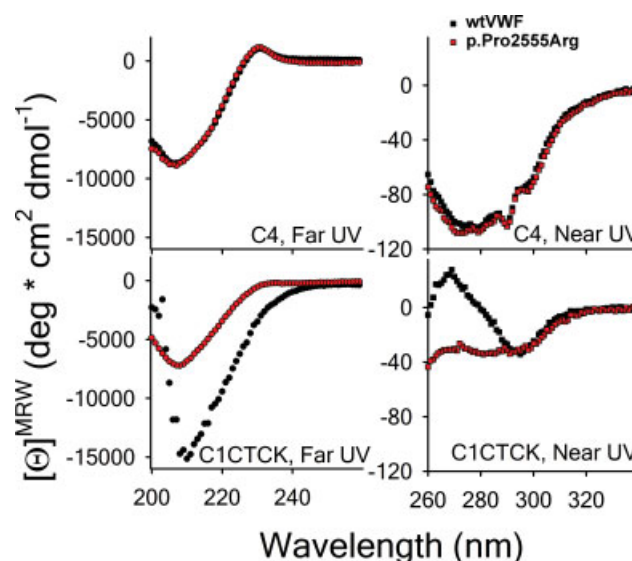
Fig. 3 Circular dichroism spectra of C4 and C1CTCK. Far-UV (*left*) and near-UV (*right*) circular dichroism spectra are shown for wild-type (●, ■) and p.Pro2555Arg (●, ■) C4 (*top*) and C1-CTCK (*bottom*). All spectra were recorded at 25°C, corrected for the signal of the corresponding buffer and converted to mean ellipticity per amino acid residue ([Θ]^{MRW}). UV, ultraviolet.

In contrast to the monomeric C4 domain, p.Pro2555Arg had a significant effect on the dimeric C1-CTCK construct, which contains the stem region of VWF (►**Fig. 3**, bottom panels). The far-UV CD spectrum shows a massive loss of secondary structure content in the mutant, which indicates an enhanced local disorder in p.Pro2555Arg C1-CTCK. An estimation of the secondary structure content using the CD spectrum deconvolution tool BeStSel[40] confirms this assessment as it reports a reduction of about 20% in ordered secondary structure content and a shift toward random coil. The near-UV CD spectrum of p.Pro2555Arg C1-CTCK also differs from that of the wt protein and indicates an altered tertiary structure.

Taken together, the CD spectra indicate that p.Pro2555Arg has no structural effect within the monomeric C4 domain, but it alters the secondary and tertiary structures of the dimeric C1-CTCK construct.

SAXS Analysis Reveals Increased Flexibility of the VWF Stem Region in p.Pro2555Arg

To further investigate the effect of the p.Pro2555Arg variant on the overall shape and size of the VWF proteins, we performed SAXS analysis on both single C4 domains and D4N-CK-dimers (►**Fig. 4** and ►**Table 2**). Similar to the results acquired from the CD spectra, the single C4 domain remains unaffected by the p.Pro2555Arg mutation. No detectable differences can be seen from the scattering curves. The Kratky plot indicates an extended fold, which agrees with the NMR structure and MD simulation shown below. Furthermore, we calculated the R_g and D_{max} values using the pairwise distance distribution function $p(r)$, which are in good agreement with the NMR structure and there is no observable difference between wt and p.Pro2555Arg. However, significant changes are visible in the context of the

Table 2 Structural parameters of VWF C4 and D4N-CK wt versus p.Pro2555Arg calculated from SAXS $p(r)$ function

	R_g[a] (nm)	D_{max}[b] (nm)
C4 wt	2.1	7.8
C4 p.Pro2555Arg	2.1	7.8
D4N-CK wt	8.8	35
D4N-CK p.Pro2555Arg	12.4	56

Abbreviations: SAXS, small-angle X-ray scattering; VWF, von Willebrand factor; wt, wild type.
[a]R_g: radius of gyration.
[b]D_{max}: maximum particle dimension.

dimeric D4N-CK domain construct. The p.Pro2555Arg mutation, as indicated by the differences in the scattering at small angles, introduces an increased size of the molecule as shown by increased R_g (1.4-fold) and D_{max} (1.6-fold) compared to wt (►**Fig. 4D**, zoomed-in inset). In line with the CD data, the mutation affects the stem structure within VWF dimers. As a possible result, the multimers could become more flexible and more accessible to GPIIb/IIIa binding upon stem opening, which could ultimately lead to increased sizes of platelet aggregates.

NMR Studies on the Isolated C4 Domain Reveal Local Distortions of the p.Pro2555Arg C4 Domain Structure and Associated Changes in Conformation Dynamics

The CD and SAXS analysis above eliminated large-scale structural changes of the isolated C4 domain as a plausible explanation for the increased AS observed in the shear flow assays. This leaves dynamics as the next candidate. Thus, we conducted NMR spin relaxation experiments on the isolated p.Pro2555Arg
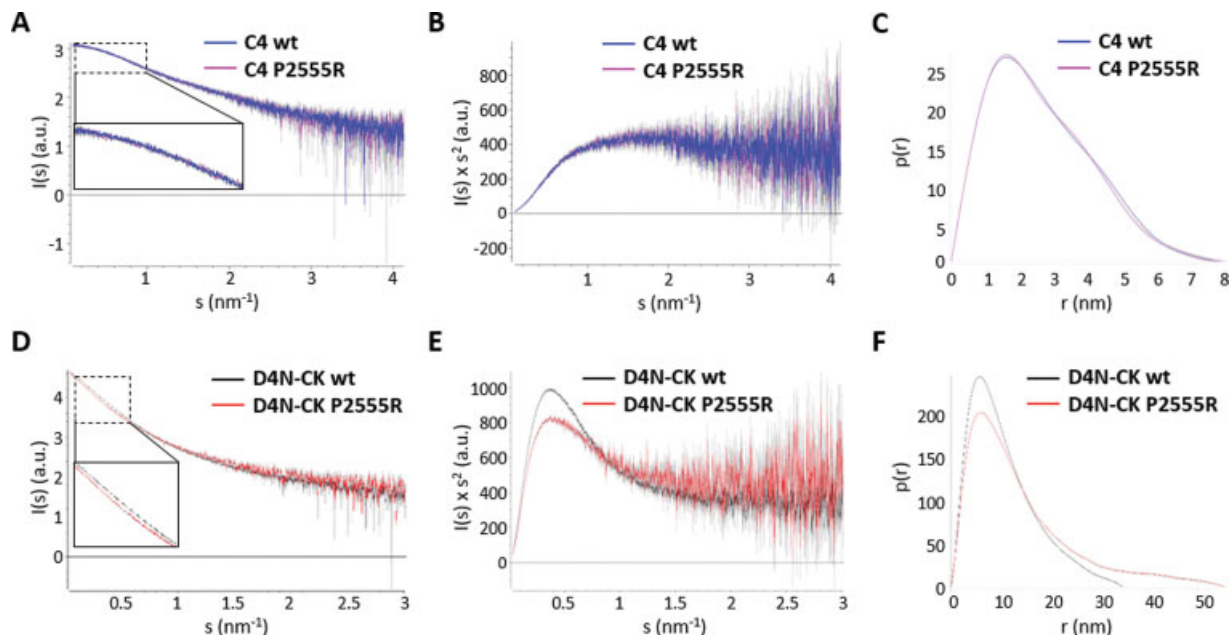
Fig. 4 SAXS showing that p.Pro2555Arg (P2555R) affects the stem structure of VWF. Scattering curve (**A**), Kratky plot (**B**), and pair distance distribution function $p(r)$ (**C**) of the single C4 domain as wt (*blue*) and p.Pro2555Arg variant (*magenta*) showing near identical profiles. For D4N-CK dimers, however, differences in the small-angle region (s < 1 nm⁻¹, zoomed-in insets) between wt (*black*) and p.Pro2555Arg (*red*) can be seen in the scattering curve (**D**) and Kratky plot (**E**), while the $p(r)$ function (**F**) shows larger D_{max} and a more flexible conformation for the p.Pro2555Arg variant compared with wtVWF. SAXS, small-angle X-ray scattering; VWF, von Willebrand factor; wt, wild type.
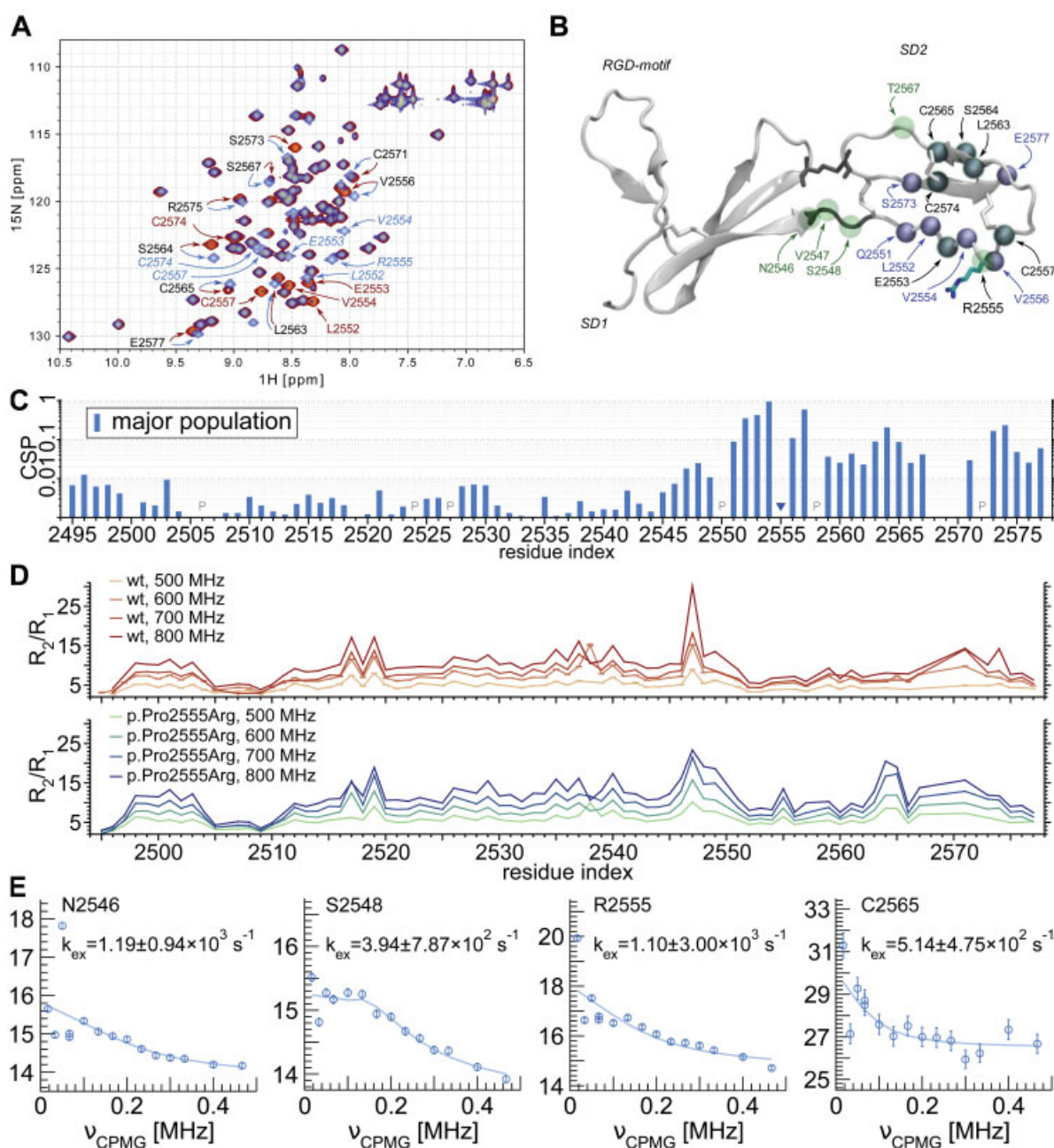
Fig. 5 NMR structural and dynamics perturbations of p.Pro2555Arg relative to wild type. (**A**) Overlapped ^{1}H–^{15}N HSQC spectra of the wild-type C4 (*red*) and p.Pro2555Arg (*blue*). Peaks with significant shifts or loss of intensity have been labeled. Slow exchange between wtVWF-like and p.Pro2555Arg-like conformations can be inferred from weak p.Pro2555Arg peaks at wild-type positions and strong peaks at p.Pro2555Arg positions. (**B**) Example of the p.Pro2555Arg structure, showing residues with significant structural perturbations (*gray-blue spheres*) and residues with millisecond dynamics switching between multiple conformations (*transparent green spheres*). (**C**) Chemicalshift perturbation (CSP) plot showing the residue-wise structural change of p.Pro2555Arg compared to wtVWF C4, where values over ∼0.05 indicate significant change in local environment. (**D**) Fast nanosecond dynamics of ^{1}H–^{15}N bonds for wtVWF (*orange-red*) and p.Pro2555Arg (*green-blue*) C4 domains, via R_2/R_1 ratios measured at four magnetic fields. (**E**) Millisecond conformation dynamics for four example residues in p.Pro2555Arg, as measured by CPMG relaxations at 800 MHz. Dynamics of 11 residues are shown in ►Supplementary Fig. S3. CPMG, Carr–Purcell–Meiboom–Gill; NMR, nuclear magnetic resonance; wtVWF, wild-type von Willebrand factor.

VWF C4 domain for comparison with published wtVWF data.[12] The comparison of the wt and p.Pro2555Arg ^{1}H-^{15}N HSQC spectra (►Fig. 5A–C) on the one hand confirms a globally unperturbed C-domain fold in agreement with the SAXS and CD data above, but on the other hand reveals subtle but extensive local perturbations throughout the three β-strand architecture of C4's SD2, indicated by shifts in multiple peak positions. Moreover, residual peak intensities at the wt locations suggest a slow conformational exchange between this distorted conformation with a wt-like minor population. Given that the wt orientation of Pro2555 points inward against the other β-strands, this suggests that Arg2555 stabilizes a distorted conformation of the entire SD2 without perturbing the overall architecture.
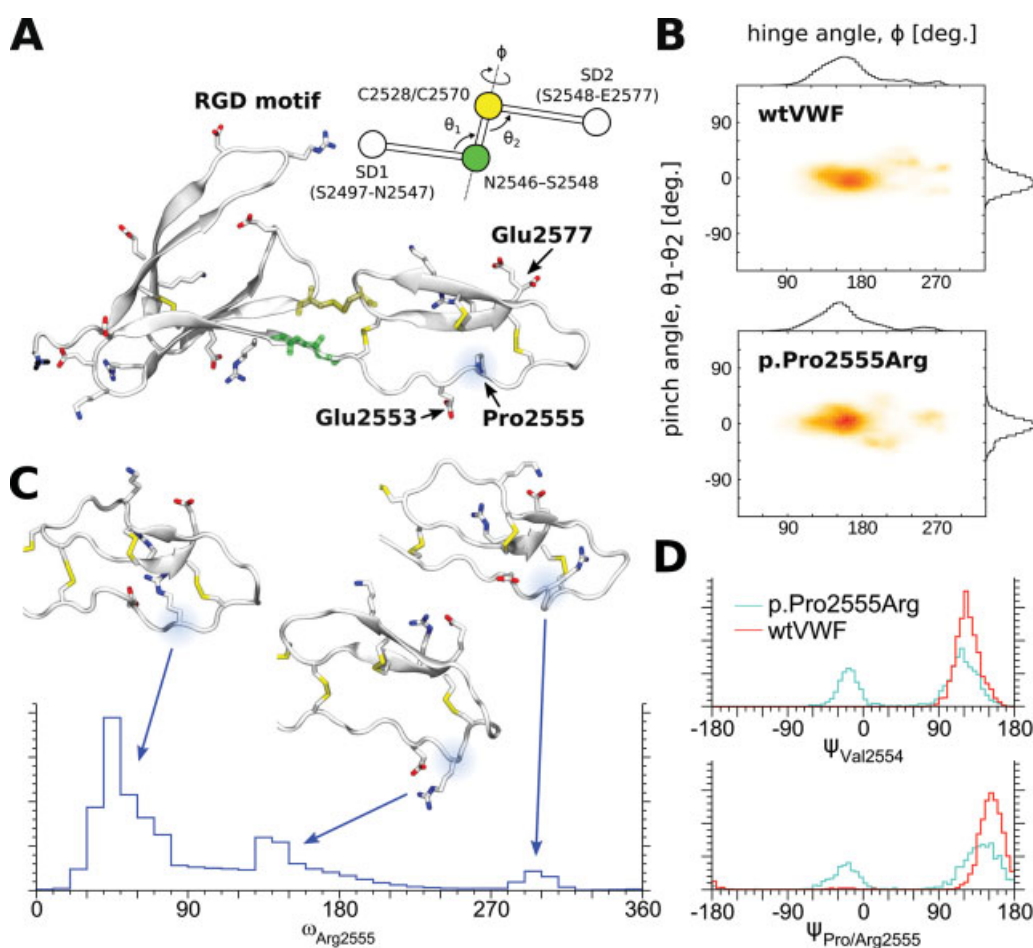
Fig. 6 Simulated global and local dynamics of wtVWF and p.Pro2555Arg C4 domains. (**A**) Representative structure of wtVWF-C4 showing its charged network, where relevant acidic, basic, and cysteine residues are displayed as sticks. C4's hinge motions are defined using four centers of mass, spanning residues 2497–2547 (most of SD1); 2546–2548 (backbone hinge joint, *green*); 2528–2570 (disulfide hinge joint, *yellow*); and 2548–2577 (SD2). The two hinge joints define an axis of rotation and SD1 defines the zero angle. (**B**) Overall conformation of C4 SD1 and SD2 for wtVWF (*upper*) and p.Pro2555Arg (*lower*) depicted using the hinge and pinch angles defined in (A). (**C**) Orientation distribution of the Arg2555 side chain relative to SD2 depicted using a dihedral angle $\omega_{Arg2555}$. The axis of rotation is defined by Val2554 and Val2556, and SD2 defines the zero angle. Each observed peak is illustrated by an example p.Pro2555Arg SD2 conformation. For a movie of an example transition from β sheet to α-helical Ramachandran of VWF-C4-p.Pro2555Arg, please refer to ►**Video 2**. (**D**) Ramachandran angle ψ distribution of Val2554 and Pro/Arg2555, showing the appearance of an α-helical backbone for p.Pro2555Arg. wtVWF, wild-type von Willebrand factor.

Local dynamics of the C4 backbone residues were further investigated in NMR ^{15}N-spin-relaxation and CPMG experiments (►**Fig. 5D, E**). The overall similarity of spin-relaxation profiles at multiple fields shows that the majority of residues remain oriented in the same direction relative to the protein. The observed isotropic tumbling times τ_c are also comparable: wt exhibits a τ_c of 7.3 ± 0.1 ns and p.Pro2555Arg exhibits a τ_c of 8.0 ± 0.1 ns. These further confirm that the extended C4 conformation is the dominant population. However, p. Pro2555Arg experiences additional and altered exchange dynamics both at the hinge and at proximal sites in SD2 (green spheres in ►**Fig. 5B**), which appear to consistently exchange on a timescale of approximately $500 \, s^{-1}$ (►**Supplementary Fig. S3**, available in the online version).

Molecular Dynamics Simulations Suggest Conformation Switching Stabilized by Alternate Arg2555 Charge Interactions

In wtVWF-C4, Pro2555 points inward into the core of SD2. Replacement of this proline by Arg2555 should therefore create steric clashes (►**Fig. 6A**). These considerations were investigated using MD simulations of p.Pro2555Arg-C4 in two independent force fields, CHARMM22* and Amber99sb-ildn*, to corroborate findings. The overall similarity of both results led us to present only the CHARMM data, with the AMBER data included in ►**Supplementary Figs. S4** to **S7** (available in the online version). We additionally include published data of wtC4 from Xu et al[12] for comparison.

The simulated trajectories confirm that p.Pro2555Arg does not perturb the relative population of extended versus bent C4 populations, as indicated by a dominant population at a hinge angle around ~180° (►**Fig. 6A, B**). These extended structures are in overall agreement with SAXS (►**Fig. 4**) and NMR (►**Fig. 5D**) data. Next, we investigated the spatial location of the long Arg2555 side chain relative to SD2. By measuring a dihedral angle $\omega_{Arg2555}$ using Val2554 and Val2556 to define the axis of rotation, we show that the Arg2555 side chain populates three distinct arrangements: behind the β-sheet and nearby the C-terminal Glu2577; pointing directly away from SD2; and a minuscule population in front of the β-sheet

(►**Fig. 6C**, ►**Video 2**). Each arrangement corresponds to a distinct charge network with neighboring SD2 residues. The conformational switching is further enabled by backbone flexibility not possible in wtVWF, where residues Val2554, Arg2555, and Val2556 exhibit α-helical conformations around Ramachandran ψ-angles of −20° (►**Fig. 6D**, ►**Supplementary Fig. S6**, available in the online version). As a consequence of the increased dynamics in the vicinity of Arg2555, the overall length of SD2 along its β-sheets is slightly contracted (►**Supplementary Fig. S7**, available in the online version). Taken together with observed NMR dynamics, p.Pro2555Arg exists in an equilibrium of at least two SD2 conformations stabilized by different charge networks.

Video 2

Example transition (0:15-0:25) from beta-sheet to alpha-helical ramachandran of VWF-C4-p.Pro2555Arg, composed using VMD and ffmpeg. Replicate #2 from 0-30ns simulation time is observed at 0.60ns/sec and 60 fps. The SD2 backbone reference frame is used to remove global motions. Trajectories have been smoothed in VMD with a half-width of 3. Protein-protein hydrogen-bonds shown as black dotted lines, using criteria of 3.0 Angs. distance and 25 degrees. Online content including video sequences viewable at: https://www.thieme-connect.com/products/ejournals/html/10.1055/a-1344-4405.

Discussion

In this study, we identified p.Pro2555Arg to be the first GOF variant of VWF which increases platelet AS. Our shear-based CPA and microfluidic assays convincingly demonstrate the underlying mechanism to be shear-force-dependent, independent of fb and mediated through interaction of the VWF stem region with platelet receptor GPIIb/IIIa via the RGD sequence in the VWF C4 domain.

Structural investigations using CD, SAXS, NMR, and MD approaches consistently support a model where the p.Pro2555Arg mutation primarily affects the structure of the VWF stem region in the context of a dimer. This points toward a mechanism where the arginine disrupts the local dimer interface and partially destabilizes the dimer organization. In the context of the multidomain VWF molecule, p.Pro2555Arg introduces a new positive charge to a local charged network comprising Glu2553, Lys2566, Arg2575, and Glu2577 in the C4 domain, as well as Arg2578 and Glu2580 at the start of C5. Together with the additional backbone flexibility permitted by the loss of Pro2555, this introduces a dynamic equilibrium between competing p.Pro2555Arg conformers seen in NMR and MD. We note that the RGD motif relevant to integrin binding lies approximately 5 nm away in SD1, which rules out a direct influence on this motif, as confirmed by static assays. Similarly, even though CD and SAXS suggest that the localized perturbation leads to a more extended and disordered VWF dimer, this is also insufficient to affect steady-state binding with GPIIb/IIIa. As the GOF mechanism for p.Phe2561Tyr, we suggested that the more extended dimers show an increase in sensitivity for stem opening compared to wtVWF dimers.[10,12] Microfluidic experiments showed that this is not the case for p.Pro2555Arg. It rather elicits an increase in AS once opening of the zipped VWF stem is accomplished. This novel effect is directly mediated by an influence of the mutation on VWF–GPIIb/IIIa interaction via the C4-RGD sequence, as blocking of the GPIIb/IIIa receptor on the platelet surface completely abolished the GOF effect of p.Pro2555Arg.

An explanation of this observed effect appears to lie indirectly in the transiently altered structure and dynamics of the C4 domain. Our NMR and MD data collected for the isolated C4 domain show preference of a subtly distorted p.Pro2555Arg C4 structure over a wt-like structure exchanging in the slow conformational exchange regime. This preference is likely to be influenced by the rest of the VWF chain as the dimer switches between zipped and open states.

Our current working hypothesis is that the distorted conformations sampled by the isolated p.Pro2555Arg-C4-domain are absent under static conditions, due to stabilization of the wt conformation by the rest of VWF. However, disruption of the resting dimer under shear flow enables distorted p.Pro2555Arg-C4 to manifest. This hinders the reformation of zipped dimers and thus indirectly increases the temporal availability of RGD domains for GPIIb/IIIa binding, leading to increased VWF–platelet crosslinking.

Our CPA experiments and a previous study by Wu et al,[34] indicated that inactivation of the VWF-RGD sequence makes more GPIIb/IIIa receptors available for binding by fb, explaining the overcompensation of platelet agglutination by fb in the CPA experiments with mutant p.Asp2509Glu. Variant p.Pro2555Arg has the same affinity for GPIIb/IIIa as wtVWF under static conditions. Therefore, one could expect that both compete out fb in the same manner; however, this is not the case. Our data suggest the following explanation for this observation: the increased temporal availability of the RGD sequence for GPIIb/IIIa binding by the p.Pro2555Arg substitution is induced by shear forces. Hence, flow conditions are required to activate the GOF effect of p.Pro2555Arg. Upon activation by the same critical shear rate as required for wtVWF, the extended lifetime of available GPIIb/IIIa-binding sites in p.Pro2555Arg leads to prolonged platelet binding. Consequently, less receptors are available for fb to bind and therefore fb is competed out more by p.Pro2555Arg than by wtVWF.

It has previously been suggested that neutrophil oxidants will render newly secreted VWF uncleavable and alter the largest plasma VWF forms to become hyperactive and resistant to proteolysis by ADAMTS13 due to methionine oxidation under inflammatory conditions.[41] Such a mechanism can, however, also be ruled out for the C4 domain as it does not contain Met residues.

In order to better connect the altered behavior in shear flow assays with our structural data, high-resolution structural and dynamics data of the C4 domain in context of longer constructs (e.g., C1-CK) would be necessary. However, this is not possible as these constructs would exceed the size limitation of NMR and are likely too flexible for other techniques such as cryo electron microscopy. Nevertheless, as the overall structure of the C4 domain is not perturbed in isolation, the mechanistic basis of the different behavior under shear flow must lie in the altered dynamics of the p. Pro2555Arg variant compared to wtVWF C4 domains investigated here by NMR and MD simulations.

The extensive similarities between wtVWF and p. Pro2555Arg functions under static conditions, echoing that of the previously published p.Phe2561Tyr report, highlight an inadequacy of such approaches for VWF research. Since many structural analyses are currently only feasible under static conditions, we strongly emphasize the necessity of incorporating variable shear flow conditions as much as possible into future assays and techniques. Investigation of the force-dependent behavior of the different variants will require future studies with a shear force chamber set-up. Such development has been initiated, for example, by utilizing a rheometer set-up or a microfluidic channel, creating shear force and pressure for in situ, time-resolved SAXS experiments.[42,43] More elaborated computational approaches could include simulating the force environment in the blood stream. As future advances expand our ability to introduce shear and elongational flow to structural investigations, we hope to fully unravel the rich secrets of this key coordinator of hemostasis.

Summarizing, our data show that the VWF stem region has specific flow-dependent functions in hemostasis in concert with GPIIb/IIIa and suggest that alteration of this interaction by mutations in the C4 domain can lead to an increase in VWF's hemostatic activity. Thus C4-domain mutants can have opposite characteristics compared with VWF variants with mutations in the other domains, which rather exhibit a decrease in hemostatic activity and thus induce the bleeding disorder VWD. Even GOF mutations in the A1 domain, counterintuitively, lead to bleeding symptoms due to spontaneous binding to platelets via GPIbα and depletion of platelets and VWF from the circulation.[44] In contrast, the presence of C4 GOF variants of VWF could increase susceptibility and/or severity for thromboembolic events as these VWF variants are hyperactive in a shear-dependent manner. For variant p.Phe2561Tyr, we indeed recently showed that it can increase the risk of early and repeated MIs by lowering the threshold for shear-induced platelet binding.[10] Variant p.Pro2555Arg does not lower this threshold but it increases temporal availability of RGD domains for GPIIb/IIIa binding compared to wtVWF and therefore enhances VWF–platelet complex formation at the normal critical shear rate. Thus, in an event which normally leads to VWF activation, i.e., vessel injury, p.Pro2555Arg might increase the risk of thrombosis. This prothrombotic GOF effect also explains why p.Pro2555Arg has not been associated with a clinical phenotype yet, as genetic analysis of VWF in general only performed in patients with bleeding symptoms.

At elevated shear rates, stable platelet aggregation is primarily dependent on VWF binding to GPIIb/IIIa.[45–47] Since vascular diseases, such as atherosclerosis and MI, are associated with increased shear rates, this interaction becomes especially important under these conditions. Furthermore, bacterial and viral infections are associated with a strong inflammatory response, which activates the endothelium thereby strongly increasing VWF levels. Recently, it has been shown that patients with COVID-19 develop hypercoagulability with elevated levels of VWF, coagulation factor VIII, and fb.[48]

After now revealing that GOF variants of VWF exist, which could even further intensify a state of hypercoagulability, it is thus of paramount importance to increase awareness of such VWF variants and to gain more mechanistic insights into the biophysics of the VWF stem region encompassing the C-domains. Further, it now becomes increasingly clear that normal functionality of the VWF stem region is of utmost importance to prevent vascular disease and thrombotic complications. Our data show that changes in the mechano-sensitivity and/or dynamics of the VWF stem can increase platelet aggregation and thus pose a risk of thromboembolic events. In the future, investigation of the VWF C4 domain should thus be considered as an additional diagnostic tool to explain such events, especially in individuals in whom they cannot be attributed to the common risk factors.

Intriguingly, our results suggest that VWF-C4 could be a promising target to develop novel strategies to treat or prevent such events. Direct inhibition of integrin receptor GPIIb/IIIa on the platelet surface blocks interaction with all protein binding partners containing RGD sequences and may cause life-threatening bleeding. The use of GPIIb/IIIa blocking antibodies as antithrombotic drugs is thus declining. Inhibiting the interaction of VWF with GPIIb/IIIa by specifically reducing binding of the VWF C4 domain to platelets could be a promising alternative.

What is known about this topic?

- It is well established that mutations in the *VWF* gene can lead to loss of hemostatic activity and von Willebrand disease.
- High antigen levels of von Willebrand factor (VWF) can possess prothrombotic properties.

What does this paper add?

- We identified p.Pro2555Arg to be the first gain-of-function variant of VWF which increases aggregate size in a shear flow- and GPIIb/IIIa-dependent manner.
- Our interdisciplinary approach reveals that the p. Pro2555Arg mutation in the C4 domain increases VWF dimer flexibility, thereby enhancing accessibility of platelet-binding sites.

Authors' Contributions

V.H. performed the microfluidic experiments, designed the microfluidic settings with S.W.S., and analyzed the dataset with C.M. and S.W.S. P.C. and J.H. designed, performed, analyzed and interpreted NMR experiments. J.H. designed, supervised, and coordinated part of this study. P.C. and C.A.-S. designed and performed the MD simulations, P.C., C.A.-S., F.K., and F.G. analyzed the MD data. E.-R.X. expressed and purified C4 and D4N-CK constructs, performed and analyzed SAXS data. M.W. contributed to analysis of the data and coordination of the study. C.V.D. designed, performed, and analyzed the GPIIb/IIIa binding experiments. A.T. and M.A. purified proteins, performed and analyzed the CD experiments. U.-K. performed and analyzed CPA experiments; G.K. and T.O. cloned and expressed VWF variants and constructs; G.K. performed cell-binding experiments, R.S. conceived, initiated, and coordinated this study; M.A.B. designed and coordinated this study and designed, supervised, and analyzed cell-binding and CPA experiments. All authors contributed in writing and editing of the manuscript.

Conflict of Interest

None declared.

References

1 Wagner DD. Cell biology of von Willebrand factor. Annu Rev Cell Biol 1990;6:217–246

2 Weiss HJ, Sussman II, Hoyer LW. Stabilization of factor VIII in plasma by the von Willebrand factor. Studies on posttransfusion and dissociated factor VIII and in patients with von Willebrand's disease. J Clin Invest 1977;60(02):390–404

3 Sadler JE, Budde U, Eikenboom JC, et al; Working Party on von Willebrand Disease Classification. Update on the pathophysiology and classification of von Willebrand disease: a report of the Subcommittee on von Willebrand Factor. J Thromb Haemost 2006;4(10):2103–2114

4 Schneppenheim R, Budde U. von Willebrand factor: the complex molecular genetics of a multidomain and multifunctional protein. J Thromb Haemost 2011;9(Suppl 1):209–215

5 Ruggeri ZM, Zimmerman TS. von Willebrand factor and von Willebrand disease. Blood 1987;70(04):895–904

6 Wieberdink RG, van Schie MC, Koudstaal PJ, et al. High von Willebrand factor levels increase the risk of stroke: the Rotterdam study. Stroke 2010;41(10):2151–2156

7 Levi M, Scully M, Singer M. The role of ADAMTS-13 in the coagulopathy of sepsis. J Thromb Haemost 2018;16(04):646–651

8 Zachariah U, Nair SC, Goel A, et al. Targeting raised von Willebrand factor levels and macrophage activation in severe COVID-19: consider low volume plasma exchange and low dose steroid. Thromb Res 2020;192:2

9 Winkelmann BR, März W, Boehm BO, et al; LURIC Study Group (LUdwigshafen RIsk and Cardiovascular Health) Rationale and design of the LURIC study–a resource for functional genomics, pharmacogenomics and long-term prognosis of cardiovascular disease. Pharmacogenomics 2001;2(01, Suppl 1):S1–S73

10 Schneppenheim R, Hellermann N, Brehm MA, et al. The von Willebrand factor Tyr2561 allele is a gain-of-function variant and a risk factor for early myocardial infarction. Blood 2019; 133(04):356–365

11 Plow EF, Pierschbacher MD, Ruoslahti E, Marguerie GA, Ginsberg MH. The effect of Arg-Gly-Asp-containing peptides on fibrinogen and von Willebrand factor binding to platelets. Proc Natl Acad Sci U S A 1985;82(23):8057–8061

12 Xu ER, von Bülow S, Chen PC, et al. Structure and dynamics of the platelet integrin-binding C4 domain of von Willebrand factor. Blood 2019;133(04):366–376

13 Müller JP, Mielke S, Löf A, et al. Force sensing by the vascular protein von Willebrand factor is tuned by a strong intermonomer interaction. Proc Natl Acad Sci U S A 2016;113(05):1208–1213

14 Legendre P, Navarrete AM, Rayes J, et al. Mutations in the A3 domain of von Willebrand factor inducing combined qualitative and quantitative defects in the protein. Blood 2013;121(11): 2135–2143

15 Legendre P, Salsmann A, Rayes J, Trassard O, Kieffer N, Baruch D. CHO cells expressing the high affinity alpha(IIb)beta3 T562N integrin demonstrate enhanced adhesion under shear. J Thromb Haemost 2006;4(01):236–246

16 Caron C, Hilbert L, Vanhoorelbeke K, Deckmyn H, Goudemand J, Mazurier C. Measurement of von Willebrand factor binding to a recombinant fragment of glycoprotein Ibalpha in an enzyme-linked immunosorbent assay-based method: performances in patients with type 2B von Willebrand disease. Br J Haematol 2006;133(06):655–663

17 Ruggeri ZM, Orje JN, Habermann R, Federici AB, Reininger AJ. Activation-independent platelet adhesion and aggregation under elevated shear stress. Blood 2006;108(06):1903–1910

18 Chen H, Fallah MA, Huck V, et al. Blood-clotting-inspired reversible polymer-colloid composite assembly in flow. Nat Commun 2013;4:1333

19 Brehm MA, Huck V, Aponte-Santamaría C, et al. von Willebrand disease type 2A phenotypes IIC, IID and IIE: a day in the life of shear-stressed mutant von Willebrand factor. Thromb Haemost 2014;112(01):96–108

20 Meyer dos Santos S, Klinkhardt U, Schneppenheim R, Harder S. Using ImageJ for the quantitative analysis of flow-based adhesion assays in real-time under physiologic flow conditions. Platelets 2010;21(01):60–66

21 Franke D, Petoukhov MV, Konarev PV, et al. *ATSAS 2.8*: a comprehensive data analysis suite for small-angle scattering from macromolecular solutions. J Appl Cryst 2017;50(Pt 4):1212–1225

22 Konarev PV, Volkov VV, Sokolova AV, et al. PRIMUS: a Windows PC-based system for small-angle scattering data analysis. J Appl Cryst 2003;36:1277–1282

23 Svergun DI. Determination of the regularization parameter in indirect-transform methods using perceptual criteria. J Appl Cryst 1992;25:495–503

24 Carr HY, Purcell EM. Effects of diffusion on free precession in nuclear magnetic resonance experiments. Phys Rev 1954;94(03): 630–638

25 Meiboom S, Gill D. Modified spin-echo method for measuring nuclear relaxation times. Rev Sci Instrum 1958;29(08):688–691

26 Tollinger M, Skrynnikov NR, Mulder FA, Forman-Kay JD, Kay LE. Slow dynamics in folded and unfolded states of an SH3 domain. J Am Chem Soc 2001;123(46):11341–11352

27 Delaglio F, Grzesiek S, Vuister GW, Zhu G, Pfeifer J, Bax A. NMRPipe: a multidimensional spectral processing system based on UNIX pipes. J Biomol NMR 1995;6(03):277–293

28 Lee W, Tonelli M, Markley JL. NMRFAM-SPARKY: enhanced software for biomolecular NMR spectroscopy. Bioinformatics 2015; 31(08):1325–1327

29 Ahlner A, Carlsson M, Jonsson BH, Lundström P. PINT: a software for integration of peak volumes and extraction of relaxation rates. J Biomol NMR 2013;56(03):191–202

30 Niklasson M, Otten R, Ahlner A, et al. Comprehensive analysis of NMR data using advanced line shape fitting. J Biomol NMR 2017; 69(02):93–99

31 Walker O, Varadan R, Fushman D. Efficient and accurate determination of the overall rotational diffusion tensor of a molecule from (15)N relaxation data using computer program ROTDIF. J Magn Reson 2004;168(02):336–345

32 Abraham AJ, Murtola T, Schulz R, et al. GROMACS: high performance molecular simulations through multi-level parallelism from laptops to supercomputers. SoftwareX 2015;1–2(September):19–25

33 König G, Obser T, Marggraf O, et al. Alteration in GPIIb/IIIa binding of VWD-associated von willebrand factor variants with C-terminal missense mutations. Thromb Haemost 2019;119(07):1102–1111

34 Wu YP, Vink T, Schiphorst M, et al. Platelet thrombus formation on collagen at high shear rates is mediated by von Willebrand factor-glycoprotein Ib interaction and inhibited by von Willebrand factor-glycoprotein IIb/IIIa interaction. Arterioscler Thromb Vasc Biol 2000;20(06):1661–1667

35 Aponte-Santamaría C, Huck V, Posch S, et al. Force-sensitive autoinhibition of the von Willebrand factor is mediated by interdomain interactions. Biophys J 2015;108(09):2312–2321

36 Huck V, Schneider MF, Gorzelanny C, Schneider SW. The various states of von Willebrand factor and their function in physiology and pathophysiology. Thromb Haemost 2014;111(04):598–609

37 Constantinescu-Bercu A, Grassi L, Frontini M, Salles-Crawley II, Woollard K, Crawley JT. Activated $\alpha_{IIb}\beta_3$ on platelets mediates flow-dependent NETosis via SLC44A2. eLife 2020;9:9

38 de Witt SM, Swieringa F, Cavill R, et al. Identification of platelet function defects by multi-parameter assessment of thrombus formation. Nat Commun 2014;5:4257

39 Deng W, Xu Y, Chen W, et al. Platelet clearance via shear-induced unfolding of a membrane mechanoreceptor. Nat Commun 2016; 7:12863

40 Micsonai A, Wien F, Kernya L, et al. Accurate secondary structure prediction and fold recognition for circular dichroism spectroscopy. Proc Natl Acad Sci U S A 2015;112(24):E3095–E3103

41 Fu X, Chen J, Gallagher R, Zheng Y, Chung DW, López JA. Shear stress-induced unfolding of VWF accelerates oxidation of key methionine residues in the A1A2A3 region. Blood 2011;118 (19):5283–5291

42 Wieland DC, Garamus VM, Zander T, et al. Studying solutions at high shear rates: a dedicated microfluidics setup. J Synchrotron Radiat 2016;23(02):480–486

43 Wieland DCF, Zander T, Garamus VM, et al. Complex solutions under shear and pressure: a rheometer setup for X-ray scattering experiments. J Synchrotron Radiat 2017;24(Pt 3):646–652

44 Ruggeri ZM. Type IIB von Willebrand disease: a paradox explains how von Willebrand factor works. J Thromb Haemost 2004;2(01):2–6

45 Kulkarni S, Dopheide SM, Yap CL, et al. A revised model of platelet aggregation. J Clin Invest 2000;105(06):783–791

46 Ruggeri ZM. Mechanisms of shear-induced platelet adhesion and aggregation. Thromb Haemost 1993;70(01):119–123

47 Ikeda Y, Handa M, Kawano K, et al. The role of von Willebrand factor and fibrinogen in platelet aggregation under varying shear stress. J Clin Invest 1991;87(04):1234–1240

48 Panigada M, Bottino N, Tagliabue P, et al. Hypercoagulability of COVID-19 patients in intensive care unit: a report of thromboelastography findings and other parameters of hemostasis. J Thromb Haemost 2020;18(07):1738–1742